

Potential energy surfaces for high-energy N + O₂ collisions

Cite as: J. Chem. Phys. 154, 084304 (2021); doi: 10.1063/5.0039771

Submitted: 6 December 2020 • Accepted: 20 January 2021 •

Published Online: 23 February 2021



Zoltan Varga,¹ Yang Liu,² Jun Li,² Yuliya Paukku,¹ Hua Guo,³ and Donald G. Truhlar^{1,a)}

AFFILIATIONS

¹Department of Chemistry, Chemical Theory Center, and Minnesota Supercomputing Institute, University of Minnesota, Minneapolis, Minnesota 55455-0431, USA

²School of Chemistry and Chemical Engineering & Chongqing Key Laboratory of Theoretical and Computational Chemistry, Chongqing University, Chongqing 401331, China

³Department of Chemistry and Chemical Biology, University of New Mexico, Albuquerque, New Mexico 87131, USA

^{a)}Author to whom correspondence should be addressed: truhlar@umn.edu

ABSTRACT

Potential energy surfaces for high-energy collisions between an oxygen molecule and a nitrogen atom are useful for modeling chemical dynamics in shock waves. In the present work, we present doublet, quartet, and sextet potential energy surfaces that are suitable for studying collisions of O₂(³Σ_g[−]) with N(⁴S) in the electronically adiabatic approximation. Two sets of surfaces are developed, one using neural networks (NNs) with permutationally invariant polynomials (PIPs) and one with the least-squares many-body (MB) method, where a two-body part is an accurate diatomic potential and the three-body part is expressed with connected PIPs in mixed-exponential-Gaussian bond order variables (MEGs). We find, using the same dataset for both fits, that the fitting performance of the PIP-NN method is significantly better than that of the MB-PIP-MEG method, even though the MB-PIP-MEG fit uses a higher-order PIP than those used in previous MB-PIP-MEG fits of related systems (such as N₄ and N₂O₂). However, the evaluation of the PIP-NN fit in trajectory calculations requires about 5 times more computer time than is required for the MB-PIP-MEG fit.

Published under license by AIP Publishing. <https://doi.org/10.1063/5.0039771>

I. INTRODUCTION

The interactions of nitrogen and oxygen species are important in atmospheric and planetary chemistry.^{1–9} In addition, these interactions are especially important for modeling shock-heated air in aerospace re-entry.^{9–23} We are developing potential energy surfaces for simulating collisions between nitrogen and oxygen species—both four-body potentials involving N₂ and O₂^{24–27} and three-body potentials involving N and O collisions with N₂ and O₂. Our initial goal, which governs the present work, is to develop the potentials needed for modeling Born–Oppenheimer collisions (i.e., collisions in which the electronic state does not change) of ground-electronic-state N, O, N₂, and O₂.^{28,29} In this work, we neglect spin-orbit coupling; therefore, the electronic spin quantum number (*S*) is conserved.

When collisions occur between collision partners with electronic degeneracy due to spatial symmetry, as in the present

case, one must consider more than one potential energy surface.³⁰ The goal of the current work is to calculate the global surfaces of the NO₂ system that are needed to describe the collisions of ground-electronic-state O₂(³Σ_g[−]) with the ground-state N atom (⁴S). Since there is no spatial degeneracy in the ground states (and spin-orbit coupling is neglected) and if we make the Born–Oppenheimer approximation, collisions occur in the lowest-energy doublet (*S* = 1/2, where *S* is the quantum number of total electronic spin), lowest-energy quartet (*S* = 1 1/2), and lowest-energy sextet (*S* = 2 1/2) spin state, and hence, we need three potentials. These are the surfaces in this paper; they all correspond to the *A'* irrep for the spatial part of the electronic wave function.

To avoid misuse of the present potentials, it is important to specify that although they are sufficient for O₂(³Σ_g[−]) + N(⁴S) collisions, they are not sufficient for NO(²Π) + O(³P) collisions. The reason for this is as follows: If one considers the collision of

ground-electronic-state NO ($^2\Pi$) with a ground-state O atom (3P) because of the higher spatial degeneracy of the collision partners, collisions occur on the six lowest doublet and six lowest quartet surfaces. The current surfaces are important for those collisions but are just a small part of the required surfaces for studying NO + O collisions. In a similar vein, we note that our previously published $N_2 + O_2$ four-body potential²⁷ is not applicable for the present purposes because the four-body potential corresponds to conservation of the four-body electronic spin, but the spins of the three-body subsystems and atomic subsystem can change when only the four-body spin is constrained. In summary, the previous $N_2 + O_2$ potential is not applicable for the present purposes, but the potentials presented here are sufficient (in the Born–Oppenheimer approximation and with neglect of spin–orbit coupling) for studying O_2 ($^3\Sigma_g^-$) + N (4S) collisions; however, the present surfaces are not sufficient for simulating experimental results on NO ($^2\Pi$) + O (3P) collisions.

Similarly, these surfaces are insufficient for a complete study of $2O + N$ intermolecular collisions, where the reactants are the separated atoms. Such three-body collisions, with all atoms in their ground electronic states, could occur—even if electronically adiabatic—on any of 18 doublet surfaces, 27 quartet surfaces, 18 sextet surfaces, and nine octet surfaces.

Nitrogen dioxide is of special interest because of its role in environmental chemistry³¹ (smog and ozone production) and in combustion processes.³² Therefore, many local or global surfaces of the doublet NO₂ system have been developed in the past three decades.^{33–49} The quartet potential of the NO₂ system was also fitted by Sayós *et al.*,⁴⁵ but as far as we know, no sextet surface has been fitted yet. It is especially important to eliminate this lacuna in our simulation database because statistically one half of the collisions of N(4S) + O₂($^3\Sigma_g^-$) occur in the sextet state with only one-third in the quartet state and one-sixth in the doublet state.

For aerospace applications, the simulations of hypersonic flow require a very high temperature range, up to 20 000 K or even 30 000 K, and our potentials are designed according to this requirement. Thus, the precise structure of the low-energy surfaces, which is very important for studying ambient-temperature processes, is less important in our consideration, and we accept a larger absolute error in fitting surfaces over a wide energy range for high-energy processes than would be desirable when fitting surfaces in a narrow energy range for low-energy applications.

In this article, two approaches were used to fit the three potentials of NO₂. The first approach is a permutationally invariant polynomial^{50,51} (PIP) fit in bond order variables to the many-body (MB) potential part of the potential, retaining only connected terms,⁵² with separate fits to the two-body parts, where the bond order variables are taken as mixed-exponential-Gaussians (MEGs).²⁴ The full name of this set of three potentials is MB-PIP-MEG, but we will use the shorthand name MEG in the rest of this article. The second approach is a permutationally invariant-polynomial neural-network (NN) fit,^{53–55} without separating the two-body and three-body parts. The full name of this set of three potentials is PIP-NN, but we will use the shorthand name NN in the rest of this article. As we know from past work⁵⁶ and as we reconfirm below for the present case, these two approaches are complementary in that the MEG fit is computationally more efficient while the NN fit has smaller fitting errors.

II. METHODS

A. Electronic structure calculations

All electronic structure calculations are performed with the 2012.1 version of the *Molpro* software package.^{57,58} We used dynamically weighted⁵⁹ state-averaged⁶⁰ complete-active-space self-consistent-field^{61,62} (DW-SA-CASSCF) calculations to obtain the multireference reference state. The active space consists of 17 electrons distributed in the 12 valence orbitals. In these DW-SA-CASSCF calculations, for each spin, three states with the same *S* were averaged (we do not need the energies of the two higher states for fitting, but including them in the calculations makes the energy of the lowest-energy state smoother as a function of geometry). The dynamical weighting factor was set to the recommended value,⁵⁹ which is 3 eV. With the lowest-energy state of the DW-SA-CASSCF calculation for the given spin state serving as the reference state, a single-state complete active space second-order perturbation theory (CASPT2) calculation was carried out with the *rs2* keyword;⁶³ this corresponds to using a level shift⁶⁴ of 0.3 hartree and to using the g4 version of the modified Fock-operator.^{65,66} The electron correlation included all the valence electrons.

The minimally augmented correlation-consistent polarized valence triple zeta basis set, *maug-cc-pVTZ*,⁶⁷ is used for all calculations.

Since a three-atom system always has a plane of symmetry, the three surfaces were constructed using electronic structure calculations carried out in *C_s* symmetry, and we found that, for all three spin states, the spatial symmetry of the lowest-energy state is *A'*.

B. DSEC method for NO₂ systems

The accuracy of calculated energies was improved by using the dynamically scaled external correlation²⁷ (DSEC) method. In the DSEC method, the parameter *F* of the original scaled external correlation (SEC) method⁶⁸ is replaced by a new parameter *p*, which is unitless and equals 1/*F*. The general equation for the DSEC energy at a given geometry is

$$E^{\text{DSEC}} = E^{\text{CASSCF}} + p(E^{\text{CASPT2}} - E^{\text{CASSCF}}), \quad (1)$$

where *p* (unlike *F*) depends on geometry. We parameterize *p* such that the DSEC relative energies agree with best estimate relative energies at key geometries. The best estimate relative energies are taken from experiment.

Let r_{NO1} , r_{NO2} , and r_{O1O2} be the three internuclear distances of the NO₂ system. We define

$$g_{1,\text{NO1}} = \begin{cases} 0 & \text{if } r_{\text{NO1}} < r_{e,\text{NO}} \\ r_{\text{NO1}} - r_{e,\text{NO}} & \text{otherwise,} \end{cases} \quad (2a)$$

$$g_{1,\text{NO2}} = \begin{cases} 0 & \text{if } r_{\text{NO2}} < r_{e,\text{NO}} \\ r_{\text{NO2}} - r_{e,\text{NO}} & \text{otherwise,} \end{cases} \quad (2b)$$

$$g_{1,\text{O1O2}} = \begin{cases} 0 & \text{if } r_{\text{O1O2}} < r_{e,\text{OO}} \\ r_{\text{O1O2}} - r_{e,\text{OO}} & \text{otherwise,} \end{cases} \quad (2c)$$

for the diatomic subsystems, and we define

$$g_{2,\text{NO1}} = \begin{cases} 0 & \text{if } r_{\text{NO1}} < r_{\text{e,NO}(\text{NO}_2)} \\ r_{\text{NO1}} - r_{\text{e,NO}(\text{NO}_2)} & \text{otherwise,} \end{cases} \quad (3a)$$

$$g_{2,\text{NO2}} = \begin{cases} 0 & \text{if } r_{\text{NO2}} < r_{\text{e,NO}(\text{NO}_2)} \\ r_{\text{NO2}} - r_{\text{e,NO}(\text{NO}_2)} & \text{otherwise,} \end{cases} \quad (3b)$$

$$g_{2,\text{O1O2}} = \begin{cases} 0 & \text{if } r_{\text{O1O2}} < r_{\text{e,OO}(\text{NO}_2)} \\ r_{\text{O1O2}} - r_{\text{e,OO}(\text{NO}_2)} & \text{otherwise,} \end{cases} \quad (3c)$$

for triatomic NO_2 , where $r_{\text{e},X}$ is an equilibrium internuclear distance given in Table I. Based on Eqs. (2) and (3), geometry-dependent weights are defined as

$$w_{1,\text{NO1}} = \exp[-a_{\text{NO}}g_{1,\text{NO1}}^2], \quad (4a)$$

$$w_{1,\text{NO2}} = \exp[-a_{\text{NO}}g_{1,\text{NO2}}^2], \quad (4b)$$

$$w_{1,\text{NO}} = \begin{cases} w_{1,\text{NO1}} & \text{if } w_{1,\text{NO1}} > w_{1,\text{NO2}} \\ w_{1,\text{NO2}} & \text{otherwise,} \end{cases} \quad (5a)$$

$$w_{1,\text{O1O2}} = \exp[-a_{\text{OO}}g_{1,\text{O1O2}}^2], \quad (5b)$$

$$w_2 = \exp[-a_{\text{NO}(\text{NO}_2)}g_{1,\text{NO1}}^2 - a_{\text{NO}(\text{NO}_2)}g_{1,\text{NO2}}^2 - a_{\text{OO}(\text{NO}_2)}g_{2,\text{O1O2}}^2], \quad (5c)$$

where a_x are parameters.

For each of the three NO_2 surfaces, the dynamically weighted scaling factor for a given geometry is

$$p = 1 + c_{(\text{O}_2+\text{N})}w_{1,\text{O1O2}} + c_{(\text{NO}+\text{O})}w_{1,\text{NO}} + c_{(\text{NO}_2)}w_2 + c_{(\text{cross})}\sqrt[3]{w_{1,\text{O1O2}}w_{1,\text{NO}}w_2}, \quad (6)$$

where $c_{(\text{O}_2+\text{N})}$ and $c_{(\text{NO}+\text{O})}$ are diatomic scaling factors, $c_{(\text{NO}_2)}$ is a triatomic scaling factor, and $c_{(\text{cross})}$ is a cross-term scaling factor.

Let E_x^{target} be the best estimate energy of geometry x , as obtained from experiment,^{69,70} and a best estimate (BE) relative energy is then defined by

$$E_{xy}^{\text{BE}} = E_x^{\text{BE}} - E_y^{\text{BE}}, \quad (7a)$$

and a DSEC relative energy is given by

$$\Delta E_{xy}^{\text{DSEC}} = E_x^{\text{CASSCF}} - E_y^{\text{CASSCF}} + p_x(E_x^{\text{CASPT2}} - E_x^{\text{CASSCF}}) + p_y(E_y^{\text{CASPT2}} - E_y^{\text{CASSCF}}). \quad (7b)$$

The BE relative energies used to obtain the parameters are collected in Table I.

First, the range parameters were obtained from Morse models, as indicated in Table II. Then, the scaling parameters were obtained from the BE energies in Table I. First, the scaling factors $c_{(\text{O}_2+\text{N})}$, $c_{(\text{NO}+\text{O})}$, and $c_{(\text{NO}_2)}$ were calculated from Eqs. (7b) and (6) for stationary structure x by taking the y structure to be the three separated atoms (where $p = 1$). Note that these scaling factors are the same for doublet, quartet, and sextet surfaces because all three potentials agree in the asymptotic regions. Then, based on these scaling factors, $c_{(\text{cross})}$ was adjusted to eliminate the effect of scaling factors $c_{(\text{O}_2+\text{N})}$ and $c_{(\text{NO}+\text{O})}$ in Eq. (6) at the stationary geometry of the doublet NO_2 structure. Although this parameter was obtained for the doublet surface, the same scaling parameters are applied consistently to all three NO_2 surfaces.

The DSEC parameters are collected in Table II. The application of the DSEC correction to the electronic structure calculations is carried out prior to the fitting procedure.

C. Selection of geometries to include in the fitting datasets

Most of the geometries used for the fits come from two grids that were used for all three spin states. In grid 1, the three atoms are placed in the O1–O2–N order. Then, the $r(\text{O1–O2})$ and $r(\text{O2–N})$ distances and the $\alpha(\text{O1–O2–N})$ angle were varied. In grid 2, the three atoms are placed in the O1–N–O2 order, and the $r(\text{O1–N})$ and $r(\text{O2–N})$ distances and the $\alpha(\text{O1–N–O2})$ angle were varied, with the restriction that $r(\text{O1–N}) \geq r(\text{O2–N})$. For these two grids, the values of the distances used are 0.8 Å–1.6 Å with a 0.1 Å increment plus 1.8 Å, 2.0 Å, 2.2 Å, 2.5 Å, 2.7 Å, 3.0 Å, 4.0 Å, and 5.0 Å, and the angles were varied from 30° to 180° with a 5° increment. The potentials for longer distances are dominated by the diatomic potentials, which are fit separately (see below).

We also carried out a multi-dimensional scan to find regions with poor data coverage. For this purpose, the Cartesian coordinates in the dataset were converted to internuclear distances. The OO internuclear distance is unique, and two NO internuclear distances were arranged in an ascending order. In the multi-dimensional scan, the OO and the shorter NO distances were varied from 0.7 Å to

TABLE I. Equilibrium distances and best-estimate relative energies (in kcal/mol) and the calculated CASPT2 relative energies before the DSEC correction (in kcal/mol).

System	State	$r_{\text{e},X}$	Best estimate	CASPT2 ^a
NO_2	X^2A_1	1.204(NO), 2.215(OO) ^b	0.0	0.0
$\text{O}_2 + \text{N}$	$^3\Sigma_g^- + ^4S$	1.208 ^c	106.9 ^d	102.7
$\text{NO} + \text{O}$	$^2\Pi + ^3P$	1.1508 ^c	74.5 ^d	77.5
$\text{O} + \text{O} + \text{N}$	$^3P + ^3P + ^4S$...	227.1 ^d	226.4

^aThe geometries were optimized by CASPT2.

^bFrom geometry optimized by CASPT2.

^cExperimental from Ref. 69.

^dExperimental from Refs. 69 and 70.

TABLE II. The parameters of the DSEC method.^a

Range parameters		Scaling factors	
a_{NO}	7.5076 ^b	$c_{(\text{O}_2+\text{N})}$	−0.012 325
a_{OO}	7.0225 ^c	$c_{(\text{NO}+\text{O})}$	0.002 178
$a_{\text{NO}(\text{NO}_2)}$	7.5076 ^b	$c_{(\text{NO}_2)}$	0.012 766
$a_{\text{OO}(\text{NO}_2)}$	2.65 ^d	$c_{(\text{cross})}$	−0.134 681

^aThe range parameters are in \AA^{-2} , and the scaling factors are unitless.^bThe square of 2.74\AA^{-1} , which is the Morse parameter of the ground-state NO molecule derived from Ref. 71.^cThe square of 2.65\AA^{-1} , which is the Morse parameter of the ground-state O_2 molecule derived from Ref. 71.^dThe square root of diatomic parameter a_{OO} .

4.0 \AA with a 0.1 \AA increment, and the longer NO was run from the actual value of the shorter NO distance to 4.0 \AA , with the three distances forming a valid triangle structure. To represent the distance between any geometries in the dataset and any geometry in the multi-dimensional scan, the absolute values of the differences of the three internuclear distance pairs (OO, shorter NO, and longer NO) were calculated and added together. If a geometry point in the multi-dimensional scan lays further than 0.33 \AA from the closest point in the dataset, then that point is considered to be in a vacant geometry region. Since the original geometry grid was already very dense, we only found 150–200 geometries for each three surfaces, and all of them were added to the set to be calculated.

After that mentioned above, the points on the grids and those resulting from the scan were augmented by additional geometries that were different for the different spin states. For example, these state-specific points are geometries close to stationary points of that given potential or geometry points used for tests specific to the given state. In these calculations, $r(\text{O1}–\text{O2})$ is fixed at 1.208 \AA , which is the equilibrium bond length of O_2 , and the $r(\text{O2}–\text{N})$ distance and the $\alpha(\text{O1}–\text{O2}–\text{N})$ angle are varied.

In some cases, points with relatively large fitting errors, as well as their surroundings, were reinvestigated to see if the error comes from wrong electronic structure calculations, since one must be extra careful as to whether multiconfigurational self-consistent field calculations have converged to the desired wave function. For this purpose, the calculations were repeated with a different set of guesses for the orbitals to attempt to get a better solution. There are many ways to generate an initial guess, and finding a good initial guess is situation-dependent. In general, an initial guess can come from a HF calculation with the same spin as the state under consideration, from a higher spin state, or from a (SA-)CASSCF calculation in which the number of states is different from that used in the actual calculation. The initial guess can be obtained at the same geometry as the actual calculation, or at a different geometry, which can be relatively far from the geometry of the actual point and possibly changed gradually along a scanning parameter (at each point of the scan, the guess comes from the previous calculation) to reach the geometry point. Trading active orbitals with virtual orbitals is also used to generate initial guesses. In certain cases, the best guess is the default option, where natural orbitals of a diagonal density matrix are constructed using atomic orbitals and atomic occupation numbers (in the present work, we have not generated initial guesses by

changing the active space, but that is another option sometimes used in previous work).

To test the surfaces, two series of trajectory calculations were carried out with the program ANT⁷² on all the NO_2 surfaces. In the first series of tests, only MEG fits were used, and trajectories were calculated for $\text{O}_2 + \text{N}$ and $\text{NO} + \text{O}$ collisions. For each spin state, we ran 500 trajectories with relative translational energies in the range 0.3 eV–4.3 eV, impact parameters in the range 0 \AA –1.6 \AA , vibrational quantum numbers in the range 1–8, and initial rotational quantum numbers in the range 3–200. For these calculations, the initial atom–diatom separation is 8 \AA , and a trajectory is terminated when any of the internuclear distances becomes longer than 9.2 \AA or if the propagation time reaches 800 fs. The Bulirsch–Stoer integrator with adaptive step size is used. All of these trajectories ran without a problem, and the geometry of every second step was saved. Then, we randomly picked ten trajectories for each potential surface (doublet, quartet, and sextet) to select 150–200 points for each spin state (the number of geometry points depends on the trajectory) for additional electronic structure calculations. The calculated and fitted energies were compared and found to be in good agreement. In particular, for the points that were calculated, the maximum deviation was less than 13 kcal/mol and the mean unsigned errors of the test fits were 2.4 kcal/mol, 3.2 kcal/mol, and 3.4 kcal/mol for the doublet, quartet, and sextet surfaces, respectively (the acceptable error level was not formulated as a hard-and-fast rule; we required smaller errors at low energy and near stationary points, but allowed larger errors on high-energy repulsive walls). Then, these points were added to the dataset to make the final fit of each NO_2 surface.

In the second series of trajectory tests, all NO_2 surfaces fitted by both NN and MEG were used. In these tests, the colliding partners are $\text{O}_2 + \text{N}$. For each surface, altogether, 1100 trajectories were run with 11 different sets of the collision energy (within range 0.2 eV–30 eV), initial vibrational quantum number (1–12) of the diatom, and initial rotational quantum number (1–24) of the diatom. The initial atom–diatom separation was set to 8 \AA . The other input parameters were the same as those for the first series. Since the trajectories did not show any odd behaviors, the fitted NN and MEG surfaces used in these tests are considered the final ones (these trajectory calculations only served to test the usability of the potentials and the geometry coverage; they are insufficient to generate cross sections or rate constants).

Based on the above-mentioned procedures, each of the spin states has a different number of points used to fit the surfaces. In particular, the datasets of the doublet, quartet, and sextet surfaces have 8434, 7818, and 8386 points, respectively. The lowest-energy point on any of the potentials is the equilibrium geometry of the doublet potential, and this will be used as the zero of energy in the rest of this article. With this zero of energy, all points used for the fits have energies below 2000 kcal/mol.

III. INTRODUCTION TO FUNCTIONAL FORMS OF THE FITS

The potential energy V for each spin state is expressed as a global function V modified with a local patch function V_{PF} ,

$$V = V_{\text{G}}(r_1, r_2, r_3) + V_{\text{PF}}(r_1, r_2, r_3), \quad (8a)$$

where r_1 denotes the O1–O2 distance, r_2 denotes the N–O1 distance, and r_3 denotes the N–O2 distance. The patch function is explained in Sec. III D. Here, we explain the global function.

The NN fit uses V_G without a many-body expansion, but the MEG fit uses the following expansion:

$$V_G = V_0 + \sum_{i=1}^3 V_{PA,Z(i)}(r_i) + V_{MB}(r_1, r_2, r_3), \quad (8b)$$

where V_0 is a constant, $V_{PA,Z}$ is a pairwise additive potential (i.e., a sum of diatomic potentials) with $Z(i) = \text{dNO}$, qNO , or OO , dNO denotes doublet NO, qNO denotes quartet NO, OO denotes triplet O_2 , and V_{MB} is the many-body term (which is a three-body term in the present application). The pairwise terms have $Z(1)$ equal to OO for all three potentials (doublet, quartet, and sextet), $Z(2)$ and $Z(3)$ equal to dNO for the doublet and quartet surfaces, and $Z(2)$ and $Z(3)$ equal to qNO for the sextet. The constant V_0 is set to 227.0 kcal/mol, which is the sum of the dissociation energy of O_2 (120.2 kcal/mol) and singlet N_2 (228.4 kcal/mol) molecules minus the dissociation energy of NO_2 (121.6 kcal/mol); this is required to make the functional form used have the zero of energy specified in the last paragraph of Sec. II C.

A. Functional form of the NN fit

For each electronic state, the following NN function form^{53–55} with two hidden layers is used:

$$V_G = b_1^{(3)} + \sum_{k=1}^K \left(w_{1,k}^{(3)} f_2 \left(b_k^{(2)} + \sum_{j=1}^J \left(w_{kj}^{(2)} f_1 \left(b_j^{(1)} + \sum_{i=1}^I w_{ji}^{(1)} G_i \right) \right) \right) \right), \quad (9a)$$

$$G_i = \hat{S} \prod_{i < j} p_{ij}^{l_{ij}}, \quad (9b)$$

where the permutation invariant polynomials^{51,73} (PIPs) are used as the input layer of the NN with the Morse like variables $p_{ij} = \exp(-\lambda r_{ij})$ (λ is a parameter adjusted to 1.0 \AA^{-1}) of internuclear distances between atoms i and j ($i, j = 1-3$); \hat{S} is a symmetrization operator that permutes the two identical oxygen atoms; I is the number of the input PIPs; J and K are the numbers of neurons in the two hidden layers; f_i ($i = 1, 2$) are nonlinear transfer functions for the two hidden layers; $w_{ji}^{(l)}$ are weights that connect the i th neuron of the $(l-1)$ th layer and the j th neuron of the l th layer; $b_j^{(l)}$ is the bias of the j th neuron of the l th layer; and the w and b variables are fitting parameters.

In the present work, the maximum order of the input PIPs is 3, resulting in 12 PIPs. The fitting parameters were optimized by nonlinear least squares fitting in which the root-mean-square error,

$$\text{RMSE} = \sqrt{\sum_{i=1}^{N_{\text{data}}} (E_{\text{output}}^i - E_{\text{target}}^i)^2 / N_{\text{data}}}, \quad (10)$$

was used to measure the performance of the fitting. The “early stopping” algorithm⁷⁴ was used to avoid overfitting with the dataset randomly divided into three parts: the training (90%), validation (5%), and test (5%) sets for each NN fitting.

Several combinations of the numbers of the neurons in NN architectures with two hidden layers were tested. Our experience has been that the improvement of fitting with a larger number of neurons is not drastic. Furthermore, the number of fitting parameters should be relatively small (less than 1/5) as a ratio to the total number of data points in the training set. As a result, we typically choose a structure with a moderate number of neurons that has a sufficiently high fitting fidelity. Based on these considerations, the final numbers of the neurons in the two hidden layers (J and K) were both chosen to be 20, resulting in 701 nonlinear fitting parameters for each potential. For each architecture, 100 NN trainings with different initial fitting parameters and different training, validation, and test sets were carried out. To minimize the random error, the final NN potential was selected as the average of three best fittings according to the NN ensemble approach.⁷⁵

The edge points randomly selected in the validation/test sets could lead to false extrapolation. Consequently, to decrease such possible errors, the fit was chosen only if all three sets have similar RMSEs. The maximum deviation is also used as a criterion for selecting the final NN potential.

Very recently, another paper appeared⁷⁶ (to be denoted VGJ) applying neural networks to fitting potential energy surfaces for aerospace applications, in particular for N_4 . Here, we contrast the approach in that work to our approach here for NO_2 and in our own previous work⁵⁶ on N_4 . The key differences are the input coordinates (permutationally invariant polynomials vs fundamental invariants), the use of separate diatomic potentials (for NO_2 , these were not used in our NN calculations, but they were used in both their and our NN work on N_4 and in all of our work with conventional least-squares fits), VGJ’s use of a tapering function to eliminate nonphysical behavior at long-range distances (for our NN fit on N_4 and for all of our work with conventional least-squares fits, we removed the non-connected terms of the permutationally invariant polynomials to improve the treatment at long range, but this was not carried out for the NN fits in the case of NO_2), VGJ’s use of relatively small networks to keep the computational costs low, our practice of averaging three fits (to further eliminate surface errors), whereas VGJ apparently did not average.

B. Diatomic potentials

Each diatomic function $V_{PA,Z}(r_i)$ has two terms that were originally introduced in Ref. 25,

$$V_{PA,Z}(r_i) = V_{SR,Z}(r_i) + V_{D3(BJ),Z}(r_i), \quad (11)$$

where the long-range term for molecule Z , $V_{D3(BJ),Z}(r_i)$, is a damped dispersion term based on Grimme’s D3 dispersion parameters with the Becke–Johnson damping (BJ) function.^{77,78} For all three diatomic potentials, the unitless parameters s_6 and s_8 are 1.0 and 2.0, respectively, and we also set $a_1 = 0.5299 \text{ a.u.}$ and $a_2 = 2.2 \text{ a.u.}$ based on Ref. 79. For the potential energy curve of the ground state of triplet O_2 ($Z = \text{O}_2$), the C_6 was fixed at $176.37 \text{ kcal}\cdot\text{\AA}^6/\text{mol}$ (C_8 is obtained from C_6); for more details, see Ref. 25. The parameters of the short-range term, $V_{SR,O_2}(r_1)$, are determined by fitting Eq. (12) to the accurate O_2 potential curve of Bytautas *et al.*⁸⁰ For $V_{SR,O_2}(r_1)$, we use the even-tempered Gaussian fitting function of Bytautas *et al.*,⁷⁹ given by

$$V_{\text{SR},\text{O}_2}(r_1) = \sum_{k=0}^7 a_k \exp(-\alpha \beta^k r_1^2), \quad (12)$$

where we obtain the coefficients a_k by linear regression and the exponent parameters α and β by nonlinear minimization. The $V_{\text{SR},\text{O}_2}(r_1)$ parameters are listed in Table III (they are also given in the supplementary materials of Refs. 25, 26, and 29).

In the case of doublet and quartet NO_2 surfaces, the potential energy curve of ground state doublet NO was used ($Z = \text{dNO}$). However, for the sextet NO_2 potential, the potential energy curve of the lowest quartet NO was used ($Z = \text{qNO}$). In both cases, the NO distances are denoted with $i = 2$ and 3 as it was mentioned above. The BE doublet NO curve, $V_{\text{PA},\text{dNO}}(r_i)$, was taken from our previous work,^{27,28} and the 230.11 kcal·Å⁶/mol C_6 parameter was used in the $V_{\text{D3(BJ)},\text{dNO}}(r_i)$ term. The other parameters of the $V_{\text{D3(BJ)},\text{dNO}}(r_i)$ term correspond to the parameters of $V_{\text{D3(BJ)},\text{O}_2}(r_i)$. The $V_{\text{SR},\text{dNO}}(r_i)$ term was refitted as a difference of terms $V_{\text{PA},\text{dNO}}(r_i)$ and $V_{\text{D3(BJ)},\text{dNO}}(r_i)$. For the fit of $V_{\text{SR},\text{dNO}}(r_i)$, Eq. (13) was used,

$$V_{\text{SR},\text{dNO}}(r_i) = B_{\text{dNO}} \left(\sum_{k=1}^{10} c_k X_{i,\text{dNO}}^k \right), \quad (13)$$

$$X_{i,\text{dNO}} = \exp(-(r_i - r_{e,\text{dNO}})/\alpha_1 - (r_i - r_{e,\text{dNO}})^2/\alpha_2), \quad (14)$$

where $r_{e,\text{dNO}}$ is the equilibrium bond length (1.1508 Å) of doublet NO. The non-linear parameters α_1 and α_2 and the B_{dNO} parameter, as well as the coefficients, c_k , were fitted, and they are collected in Table IV.

In the case of the quartet NO curve, $V_{\text{PA},\text{qNO}}(r_i)$, CASPT2 calculations (with the g4 option, a level shift of 0.3 hartree, and the two 1 s orbitals excluded from the electron correlation) were carried out based on SA(3)-CASSCF(8o,13e) reference wave function, where the spin state was set to quartet, the three states were dynamically weighted, and C_s symmetry was applied. The NO distance was scanned from 0.6 Å to 10.47 Å, by a 0.01 Å increment. Based on the dissociation energy of the doublet NO ($D_{e,\text{dNO}} = 152.6$ kcal/mol) and the T_e (109.9 kcal/mol)⁸¹ energy between the $X^2\Pi$ and $a^4\Pi$ states, the dissociation energy of a $^4\Pi$ state was calculated, and this BE energy was used in the static version of Eq. (7) to get the scaled external correlation, i.e., the original SEC, where $p_x = p_y = 1.13$. Since the $a^4\Pi$ state dissociates to the same limit as the $X^2\Pi$ state, we

TABLE III. Re-optimized parameters for the short-range term, $V_{\text{SR},\text{O}_2}(r_1)$, for the diatomic O_2 potential.

Parameter (unit)	Value
α (Å ⁻²)	$9.439\,784\,362\,354\,936 \times 10^{-1}$
β (-)	1.262 242 998 506 810
a_0 (millihartree)	$-1.488\,979\,427\,684\,798 \times 10^3$
a_1 (millihartree)	$1.881\,435\,846\,488\,955 \times 10^4$
a_2 (millihartree)	$-1.053\,475\,425\,838\,226 \times 10^5$
a_3 (millihartree)	$2.755\,135\,591\,229\,064 \times 10^5$
a_4 (millihartree)	$-4.277\,588\,997\,761\,775 \times 10^5$
a_5 (millihartree)	$4.404\,104\,009\,614\,092 \times 10^5$
a_6 (millihartree)	$-2.946\,204\,062\,950\,765 \times 10^5$
a_7 (millihartree)	$1.176\,861\,219\,078\,620 \times 10^5$

TABLE IV. Re-optimized parameters for the short-range term, $V_{\text{SR},\text{dNO}}(r_i)$, for diatomic doublet NO potential.

Parameter	Value
α_1 (Å)	0.896 601 839 395 554
α_2 (Å ²)	2.069 542 710 330 37
B_{dNO} (kcal/mol)	-149.478 44
c_1	-0.138 534 305 380 708
c_2	1.889 990 874 379 91
c_3	-4.297 653 558 650 66
c_4	21.430 539 556 708 7
c_5	-44.347 827 069 026 3
c_6	41.072 408 288 420 3
c_7	-10.909 962 575 954 4
c_8	-10.687 260 815 907 1
c_9	9.189 735 457 956 48
c_{10}	-2.201 965 266 358 97

assume that the long-range term in Eq. (11) is very similar for these two states. Therefore, the parameters set for $V_{\text{D3(BJ)},\text{dNO}}(r_i)$ are used for the term of $V_{\text{D3(BJ)},\text{qNO}}(r_i)$ as well. Then, the $V_{\text{SR},\text{qNO}}(r_i)$ term was fitted as a difference of terms $V_{\text{PA},\text{qNO}}(r_i)$ and $V_{\text{D3(BJ)},\text{qNO}}(r_i)$. For the fit of $V_{\text{SR},\text{qNO}}(r_i)$, Eq. (15) was used,

$$V_{\text{SR},\text{qNO}}(r_i) = B_{\text{qNO}} \left(\sum_{k=1}^{10} c_k X_{i,\text{qNO}}^k \right), \quad (15)$$

$$X_{i,\text{qNO}} = \exp(-(r_i - r_{e,\text{qNO}})/\alpha_1 - (r_i - r_{e,\text{qNO}})^2/\alpha_2). \quad (16)$$

Here, $r_{e,\text{qNO}}$ is the equilibrium bond length (1.4219 Å)⁵² of a $^4\Pi$ NO. The parameter B_{qNO} was fixed at 42.7 kcal/mol. The non-linear parameters α_1 and α_2 , as well as the coefficients, c_k , were fitted, and they are collected in Table V.

TABLE V. Optimized parameters for short-range term, $V_{\text{SR},\text{qNO}}(r_i)$, for diatomic quartet NO potential.

Parameter	Value
α_1 (Å)	0.512 278 626 249 86
α_2 (Å ²)	1.122 416 809 737 78
c_1	-0.803 736 202 408 199
c_2	12.803 364 029 556 2
c_3	-38.692 021 976 777 6
c_4	69.709 031 444 894 8
c_5	-77.248 460 068 776 5
c_6	49.276 565 279 387 6
c_7	-15.248 280 905 310 6
c_8	0.323 472 459 125 756
c_9	0.990 405 801 350 144
c_{10}	-0.174 629 129 756 616

C. Many-body potential of the MEG fit

The many-body term of the potential energy is expressed as

$$V_{\text{MB}}(r_1, r_2, r_3) = \sum_{\substack{\text{connected,} \\ n_1+n_2+n_3}}^l D_{n_1 n_2 n_3} S[X_1^{n_1} X_2^{n_2} X_3^{n_3}], \quad (17)$$

where $S[\dots]$ is a permutationally invariant polynomial basis function obtained by symmetrization of a primitive monomial basis function, as also used by Xie and Bowman.^{50,51} The restriction to connected terms was introduced in Ref. 82. For all three potentials, twelfth-order ($l = 12$) many-body functions were used. The bond order variables, X_i , are mixed-exponential-Gaussian functions,²⁴

$$X_i = \exp[-(r_i - r_{e,Z})/a_Z - (r_i - r_{e,Z})^2/b_Z], \quad (18)$$

where a_Z , a_Z , and $r_{e,Z}$ (Z is either O_2 or NO) are nonlinear parameters collected in Table VI.

As we already used recently for fitting the N_2O and O_3 surfaces,^{28,29} the four-body frame of a general A_2B_2 system was applied. Considering this general scheme as an O_2N_2 system, one of the N atoms was placed far apart from the other three atoms.

To carry out of the fit of the many-body term, the following error function is minimized:

$$F = \sum_{j=1}^n W_j (V_j^{0,\text{PA}} - V_j + \sum_{k=1}^m d_k s_{jk})^2, \quad (19)$$

with respect to the linear coefficients d_k , where m and n are the number of basis functions and the number of fitted data points, respectively, $V_j^{0,\text{PA}}$ is the sum of the constant and pairwise terms at geometry point j , V_j is the energy of geometry point j , d_k is the k th $D_{n_1 n_2 n_3}$ coefficient, s_{jk} is the k th basis function $S[X_1^{n_1} X_2^{n_2} X_3^{n_3}]$ evaluated at geometry point j , and W_j is a weighting function used to avoid too much emphasis on the high-energy data points,

$$W_j = \begin{cases} 1 & \text{for } V_j \leq (E_c + E_{sh}) \\ [(E_c + E_{sh})/V_j]^p & \text{for } V_j > (E_c + E_{sh}), \end{cases} \quad (20)$$

where E_c is a parameter of the fitting process that reduces the weights of very-high-energy data points. Parameter E_{sh} is arbitrarily set equal to 121.6 kcal/mol, which is the energy difference of stationary points $\text{N}_2 + \text{O}_2$ and $\text{NO}_2 + \text{N}$, i.e., the difference between the reference energies of the four- and three-body frames. We chose E_c and the power p to be 227.0 kcal/mol and 1.5, respectively, for all three NO_2 fits.

TABLE VI. The nonlinear parameters of the many-body MEG variables for the NO_2 surfaces.

Surface	Z	$r_{e,Z}$ (Å)	a_Z (Å)	b_Z (Å ²)
Doublet	O_2	1.208	1.350	2.75
	NO	1.1508	1.150	2.75
Quartet	O_2	1.208	0.97	1.51
	NO	1.1508	0.75	1.30
Sextet	O_2	1.208	1.25	2.10
	NO	1.4219	0.94	3.90

The doublet, quartet, and sextet MEG surfaces of NO_2 were fitted by a modified version of our *PIPFit* program.⁸³

D. Patch functions for the MEG and NN fits

Test fits showed that the functional forms of the terms described so far are not flexible enough to properly fit the barrier between the 2A_1 and 2B_2 minima of doublet NO_2 .

We first consider the MEG fit. We originally used a 10th-order MEG fit [$l = 10$ in Eq. (17)], and increasing this to a 12th-order fit did not solve the problem (we have not seen signs of overfitting at the 12th order, but going to higher order could be risky in that regard). The switching of the 2A_1 and 2B_2 states is only a few kcal/mol higher in energy than the energy of the minimum energy structure of the 2B_2 state, and the crossing seam of these states is also very close to the minimum energy structure of 2B_2 . Since the MEG fitting function does not have the flexibility to follow the proper shape of these states, the location of the 2B_2 structure rather appears as a shoulder instead of a well. To restore the barrier and give a well shape of the surface around the 2B_2 structure, we added a local patch function, $V_{\text{PF}}(r_1, r_2, r_3)$, to the doublet NO_2 potential,

$$V_{\text{PF}}(r_1, r_2, r_3) = a_0 \exp[Y(r_1, r_2, r_3)], \quad (21)$$

$$Y(r_1, r_2, r_3) = -(r_2 - r_{\text{fp}})^2/a_1 - (r_3 - r_{\text{fp}})^2/a_1 - [(r_2^2 + r_3^2 - r_1^2)/(2r_2r_3) - \cos\theta_{\text{fp}}]^2/a_2. \quad (22)$$

The parameters of the patch function are collected in Table VII. The first two terms on the right-hand side of Eq. (22) correspond to the two N–O distances. By plotting the potential in the geometry region near the crossing seam of the 2A_1 and 2B_2 states close to the minimum of the 2B_2 state, we found that using the O–N–O angle (α_1) is more straightforward than using the O–O distance to describe the shape of the crossing seam. Therefore, the third term on the right-hand side of Eq. (22) uses the deviation of O–N–O angle from a fixed angle. Nevertheless, this patch function was parameterized such that it decreases very quickly as the bond lengths start deviating from the focus point (defined by r_{fp} and θ_{fp}). Figure 1 shows an example cut with three sets of data: the target DSEC-CASPT2/maug-cc-pVTZ energies, the fitted MEG surface without the patch function, and the fitted MEG surface with the patch function.

When the NN fits were used, we found the same problem. The NN fit has a better performance than that of the MEG fit, i.e., the energies of the NN fit lie closer to the energies in the dataset,

TABLE VII. Parameters of the patch functions of the doublet NO_2 surfaces.

Parameter (unit)	MEG	NN
a_0 (kcal/mol)	5.0	3.0
a_1 (Å ²)	0.010	0.008
a_2 (unitless)	0.002	0.0008
r_{fp} (Å)	1.25	1.25
θ_{fp} (deg)	107.0	107.0

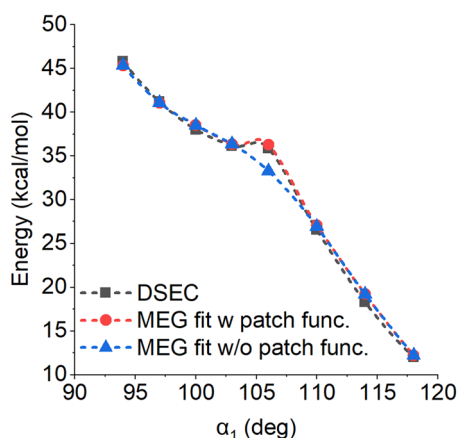


FIG. 1. An example ($r_2 = r_3 = 1.25$ Å) showing the effect of the patch function on the MEG fit to the doublet surface.

but the cusp of the state crossing of the 2A_1 and 2B_2 states is still cut off. Thus, this patch function was also added to the NN fit, but with a different set of parameters, which are also given in Table VII.

For the quartet and sextet NO_2 surfaces, such patch functions are not needed, and they were not applied.

IV. RESULTS AND DISCUSSION

The fitting errors of the NN and MEG fits are collected in Table VIII, in which the mean unsigned errors (MUEs) and root-mean-square errors (RMSEs) are shown for various energy ranges, as well as for the entire (2000 kcal/mol) energy range [recall that all energies are relative to the equilibrium energy of NO_2 (2A_1)]. Although the order of the many-body part in the MEG fits increased to 12 from the previously used 9 (for N_4) or 10 (for all other systems), the MEG fits are still unable to match the performance of the NN fits. This observation is consistent with our recent comparison of the N_4 potential using different fitting techniques,⁵⁶ and it is attributable to the ultra-flexibility^{84–87} of the NN functional form.

Table IX compares the current fits for NO_2 to some of our previous fits for similar systems, in particular to the $1^1A'$, $1^1A''$, $1^3A'$, $1^3A''$, $1^5A'$, and $1^5A''$ surfaces of O_3 ²⁹ and the $3^3A'$ and $3^3A''$ surfaces of N_2O .²⁸ The error of the MEG fit of $^2A'$ of NO_2 is about half that of the MEG fit of the $1^1A'$ and $1^1A''$ surfaces of O_3 . There is another approximate halving of the error in going to the NN fit. For the surface with middle spin state, the improvement of the quartet NO_2 surface compared to the triplet O_3 and NO_2 surfaces is less than that in the singlet and doublet surfaces; the MUE of the $^4A'$ surface of NO_2 is about 70% of the average MUE of the two triplet O_3 surfaces and about 90% of the two triplet N_2O surfaces. For this $^4A'$ surface of NO_2 , the MUE of the NN fit is 1/3 of that of the MEG fit. The MUEs of the current and previous MEG fits are similar for the high-spin-state surfaces. The performance of the NN fit is outstanding for the $^6A'$ surface of NO_2 , and the MUE of the NN fit is about 1/6th of that of the MEG fit.

TABLE VIII. Mean unsigned error (MUE) and root-mean-square error (RMSE) of the fitted potential energy surfaces with respect to DSEC-CASPT2/maug-cc-pVTZ results for various energy ranges (in kcal/mol).

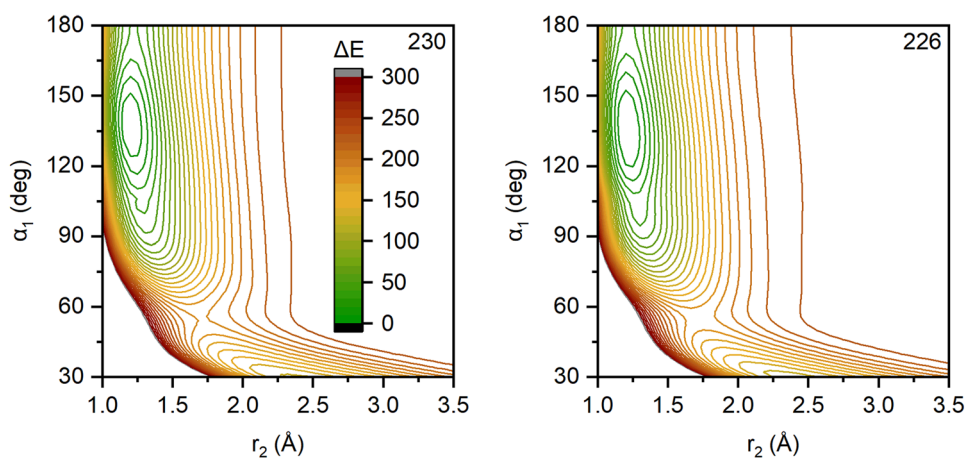
Energy range	Number of points	NN		MEG	
		MUE	RMSE	MUE	RMSE
Doublet					
$0 \leq E < 100$	1664	0.8	1.3	1.3	1.9
$100 \leq E < 200$	3559	0.8	1.4	1.2	1.8
$200 \leq E < 400$	2177	0.8	1.8	1.6	2.6
$400 \leq E < 1000$	880	1.6	2.5	4.2	5.8
$1000 < E > 1850$	154	2.3	3.5	8.6	10.8
All data	8434	0.9	1.7	1.8	3.1
Quartet					
$76 < E < 100$	443	0.3	0.4	0.9	1.3
$100 \leq E < 200$	3769	0.7	1.2	2.0	2.7
$200 \leq E < 400$	2277	0.7	1.4	2.0	2.7
$400 \leq E < 1000$	1107	1.7	2.9	3.8	5.4
$1000 < E > 1914$	222	2.2	3.5	10.3	14.3
All data	7818	0.8	1.7	2.4	4.0
Sextet					
$106 \leq E < 200$	2493	0.3	0.4	1.5	2.0
$200 \leq E < 400$	3800	0.6	1.0	2.6	4.1
$400 \leq E < 1000$	1728	0.8	1.4	5.5	8.1
$1000 \leq E < 1998$	365	0.7	1.1	7.3	9.8
All data	8386	0.5	1.0	3.1	5.1

Some of the improvements in the current fits are due to the fact that the fits of the NO_2 surfaces used significantly more points than were used in the previous O_3 and N_2O surfaces. Since the O_3 system has a higher permutation symmetry than the other two systems, one expects to require lower number of points for that system than for the others; however, the fits of the NO_2 surfaces also used about 3.5 times more points than those used for the N_2O surfaces, although both have the same permutational symmetry. Not only does having more points in the fitting datasets improve the quality of the fits for a given order of polynomial but also it allows the application of higher order without overfitting; thus, the present fits used $l = 12$, whereas we used many-body functions with $l = 9$ for our N_4 fit and $l = 10$ for all our other fits prior to the present work.

Table IX also compares the data distribution in the energy bins for the O_3 , N_2O , and NO_2 systems. For the O_3 system, the general trend is that the number of points used was a continuously decreasing function of the bin energy. Also, as the spin increased from low to high, the relative contribution of the higher energy bins increased since higher spin states are usually more repulsive than the lower spin states, and the energies of all spin states are given relative to the global energy minimum, which belongs to the deepest energy well of the lowest spin state. The middle or high spin states usually do not have such deep wells as can be seen, for instance, in Figs. 7, 10, and 13 of Ref. 29 for O_3 or later in this article for NO_2 . In the cases of NO_2 and N_2O , this trend with spin state is the same as that for O_3 , but the number of points does not monotonically decrease as a function of bin energy. In the article on O_3 ,²⁹ the fitting errors suggested that a fit becomes easier and more accurate for higher spin states.

TABLE IX. Comparison of the mean unsigned error (MUE), the number of points, and the distribution of points in the different energy bins (in kcal/mol) of the current fits of NO₂ and our previous fits of O₃ and N₂O.

	Low spin		Middle spin		High spin	
O ₃ ^a	1 ¹ A'	1 ¹ A''	1 ³ A'	1 ³ A''	1 ⁵ A'	1 ⁵ A''
MUE: MEG (<i>l</i> = 10)	4.0	3.3	3.6	3.1	3.4	2.9
Number of points	1686	1622	1645	1605	1617	1587
0 ≤ <i>E</i> < 100 (%)	56	50	48	50	36	35
100 ≤ <i>E</i> < 200 (%)	18	21	21	21	27	26
200 ≤ <i>E</i> < 500 (%)	15	13	15	15	17	18
500 ≤ <i>E</i> < 1000 (%)	8	13	12	11	15	14
1000 < <i>E</i> (%)	3	3	4	3	5	6
N ₂ O ^b			3 ³ A'	3 ³ A''		
MUE: MEG (<i>l</i> = 10)			2.9	2.5		
Number of points			2298	2280		
0 ≤ <i>E</i> < 100 (%)			25	26		
100 ≤ <i>E</i> < 200 (%)			49	46		
200 ≤ <i>E</i> < 350 (%)			19	20		
350 ≤ <i>E</i> < 1000 (%)			6	8		
1000 < <i>E</i> (%)			0.2	0.3		
NO ₂	2 ² A'			4 ⁴ A'		
MUE: MEG (<i>l</i> = 12)	1.8			2.4		
MUE: NN	0.9			0.8		
Number of points	8434			7818		
0 ≤ <i>E</i> < 100 (%)	20			6		
100 ≤ <i>E</i> < 200 (%)	42			48		
200 ≤ <i>E</i> < 400 (%)	26			29		
400 ≤ <i>E</i> < 1000 (%)	10			14		
1000 < <i>E</i> (%)	2			3		

^aReference 29.^bReference 28.**FIG. 2.** Contour map of ²A' potential of NO₂, where *r*₃ = *r*₂. The increment in the contours is 10 kcal/mol; the energies are 0 kcal/mol–300 kcal/mol (left—MEG, right—NN). The energy of the plateau is added at the upper right corner.

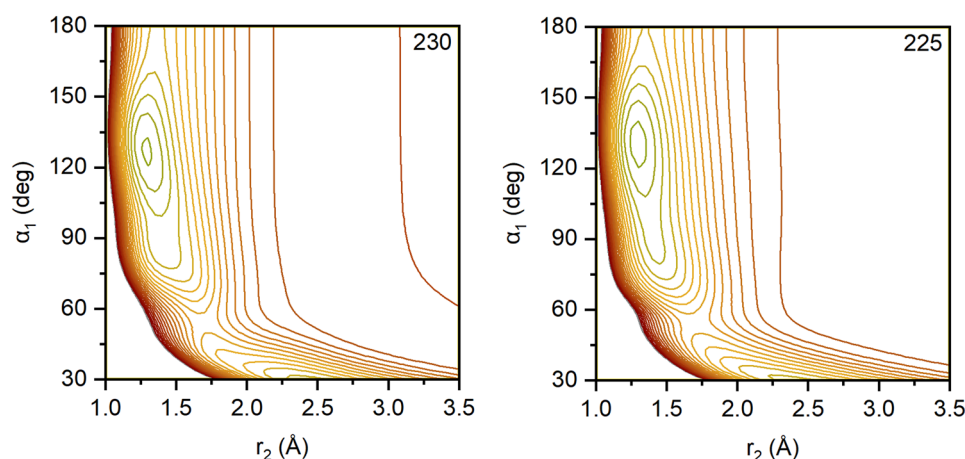


FIG. 3. Contour map of $4A'$ potential of NO_2 , where $r_3 = r_2$. The increment in the contours is 10 kcal/mol; the energies are 0 kcal/mol–300 kcal/mol (left—MEG, right—NN). The energy of the plateau is added at the upper right corner.

This could be rationalized since a higher spin state surface is—in general—more repulsive than a lower spin state surface and usually has lower number of minima. This same trend is observed for the NN fits of the NO_2 surfaces, but it is reversed for the MEG fits of the NO_2 surfaces.

Figures 2–13 are contour plots of the $2A'$, $4A'$, and $6A'$ surfaces, where the left and right panels are the MEG and the NN fits, respectively. As a reminder, r_1 is the O–O distance and r_2 and r_3 are the two N–O distances; the O–N–O and N–O–O bond angles are α_1 and α_2 , respectively.

TABLE X. Optimized coordinates and energies of selected structures of the MB-PIP-MEG and PIP-NN fits.^a

Structure	Fit	r_1 (Å)	r_2 (Å)	r_3 (Å)	α_1 (deg)	α_2 (deg)	V (kcal/mol)
D1-min	MEG		1.201	1.201	137.3		0.0
($2A_1$ minimum)	NN		1.214	1.214	135.4		0.0
D2-min	MEG		1.286	1.286	104.1		36.8
($2B_2$ minimum)	NN		1.286	1.286	105.0		33.9
D3-ts	MEG		1.221	1.221	180.0		38.8
	NN		1.212	1.212	180.0		36.9
D4-sts	MEG		1.710	1.710	54.9		179.4
	NN		1.719	1.719	55.0		175.6
D5-min	MEG	1.933	1.148			124.8	70.9
	NN	1.985	1.145			124.5	68.7
D6-sts	MEG	1.257	1.634			180.0	141.4
	NN	1.246	1.616			180.0	139.2
Q1-min	MEG		1.291	1.291	126.4		88.0
	NN		1.294	1.294	130.6		85.8
Q2-sts	MEG		1.361	1.361	180.0		127.1
	NN		1.344	1.344	180.0		129.2
Q3-sts	MEG		1.695	1.695	54.0		162.3
	NN		1.694	1.694	54.4		163.8
S1-min	MEG		1.343	1.778	180.0		190.2
	NN		1.308	1.773	180.0		186.3
S2-ts	MEG		1.548	1.548	180.0		194.8
	NN		1.565	1.565	180.0		191.6
S3-(s)ts	MEG		1.875	1.875	58.3		223.1
	NN		1.828	1.828	57.5		224.0

^aThe names are given in format $mn-c$, where m is the first letter of the multiplicity (D, Q, or S), n is the serial number of the structure, and c is the character of the stationary point; min—minimum, ts—transition structure, and sts—second-order transition structure (hilltop). Coordinate r_1 is the O–O distance, and r_2 and r_3 are the two N–O distances; the O–N–O and N–O–O bond angles are α_1 and α_2 , respectively.

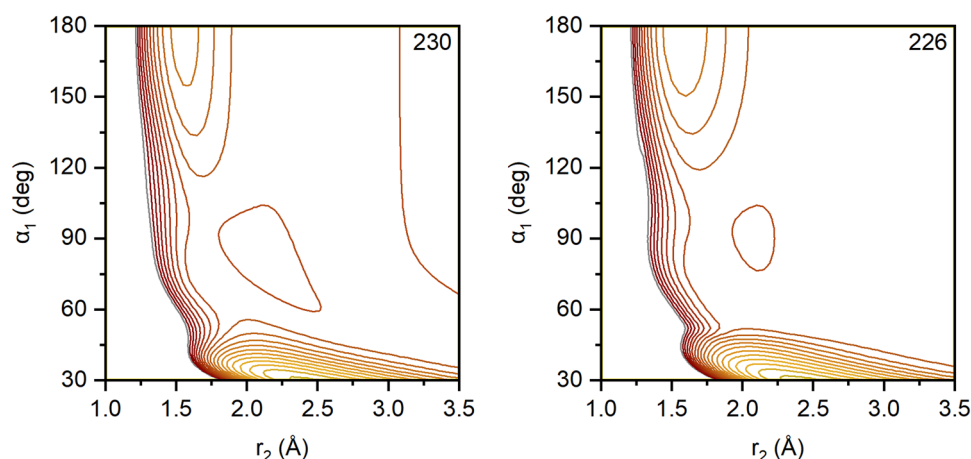


FIG. 4. Contour map of ${}^6A'$ potential of NO_2 , where $r_3 = r_2$. The increment in the contours is 10 kcal/mol; the energies are 0 kcal/mol–300 kcal/mol (left—MEG, right—NN). The energy of the plateau is added at the upper right corner.

In Figs. $2({}^2A')$, $3({}^4A')$, and $4({}^6A')$, the α_1 angle is varied from 30° to 180° and the two N–O distances ($r_2 = r_3$) are varied from 1.0 Å to 3.5 Å. In these three figures, the region of O_2 is well separated from N ($\alpha_1 < 45^\circ$ and longer N–O distances), and the three surfaces are nearly identical because the interaction of $\text{O}_2({}^3\Sigma_g^-)$ with the N atom (4S) has not yet split the spin states. For shorter N–O distances and larger α_1 angle, the three surfaces are very different; next, we consider these regions of stronger interaction.

The dominant feature in this region of the doublet surface is the well of ground-state NO_2 (2A_1). The geometry of the minimum-energy structure, as optimized by the *Polyrate* program⁸⁸ with the fitted surfaces, is given in Table X as structure D1-min. The small well of the 2B_2 structure (D2-min in Table X) only appears in Fig. 2 as a small distortion of the contours at $\alpha_1 \approx 100^\circ$, and it makes the dominant well of the 2A_1 structure somewhat asymmetric. At $\alpha_1 = 180^\circ$, there is a transition structure (D3-ts) that connects two D1-min structures. The wells in the NO_2 region and the region of $\text{O}_2 + \text{N}$ are separated by a relatively high barrier; in Fig. 2, a second-order transition structure (D4-sts) is the lowest energy point of this barrier.

One can see a well in the quartet surface (Fig. 3) in the NO_2 region, similar to the doublet well (Fig. 2), but the quartet well is not as deep. Table X has the coordinates of the minimum structure Q1-min, and in Fig. 3, the top of the inversion barrier at $\alpha_1 = 180^\circ$ is a second-order transition structure (Q2-sts), unlike the case in Fig. 2. To get an inversion transition structure between two Q1-min minima, we attempted to keep the bending imaginary frequency of the linear and symmetric Q2-sts structure by making the two NO distances different. For small or moderate distortion of the two NO bond lengths, the optimization led back to Q2-sts, and for significant distortion, the longer NO bond broke.

As on the doublet surface, the wells in the NO_2 region and the region of $\text{O}_2 + \text{N}$ are separated by a relatively high barrier on the quartet surface, and the geometry of the second-order transition structure (Q3-sts) of the quartet surface is very similar to that of D5-sts of the doublet surface.

In the plots of Fig. 4 (in which the two NO distances are kept equal), the sextet surface also shows a shallow well in the NO_2 region centered around a linear transition structure (S1-ts), which leads to an asymmetric linear minimum, S2-min, with different NO

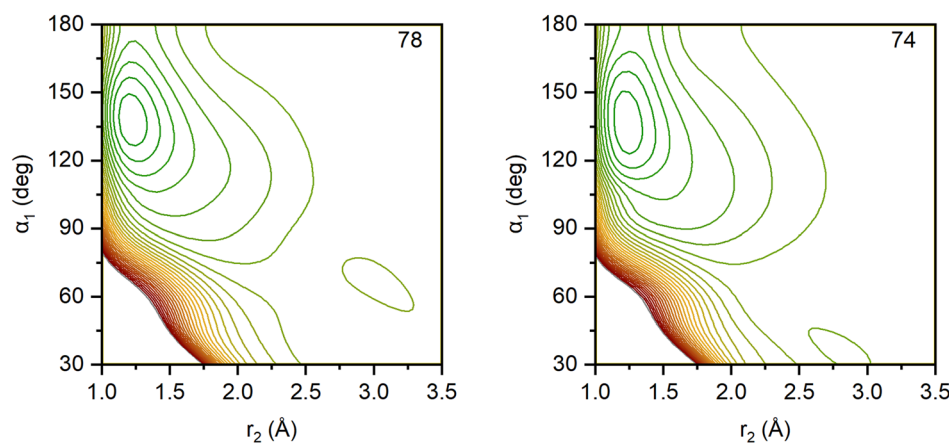


FIG. 5. Contour map of ${}^2A'$ potential of NO_2 , where $r_3 = 1.151$ Å. The increment in the contours is 10 kcal/mol; the energies are 0 kcal/mol–300 kcal/mol (left—MEG, right—NN). The energy of the plateau is added at the upper right corner.

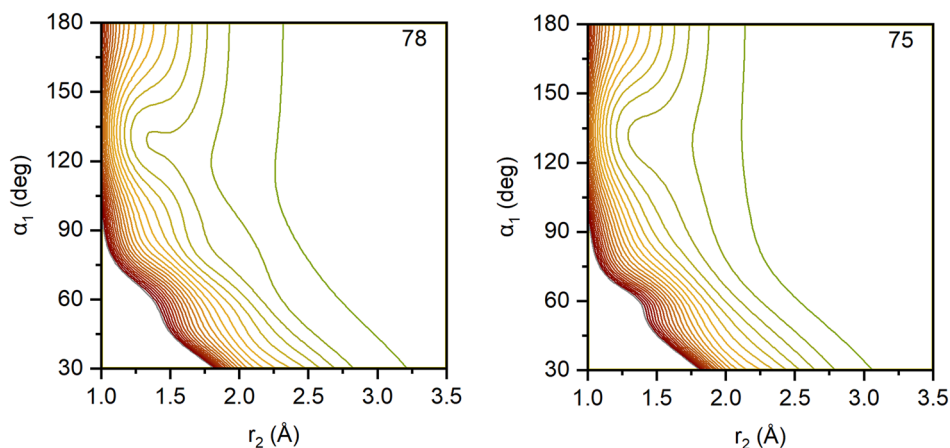


FIG. 6. Contour map of $4A'$ potential of NO_2 , where $r_3 = 1.151 \text{ \AA}$. The increment in the contours is 10 kcal/mol; the energies are 0 kcal/mol–300 kcal/mol (left—MEG, right—NN). The energy of the plateau is added at the upper right corner.

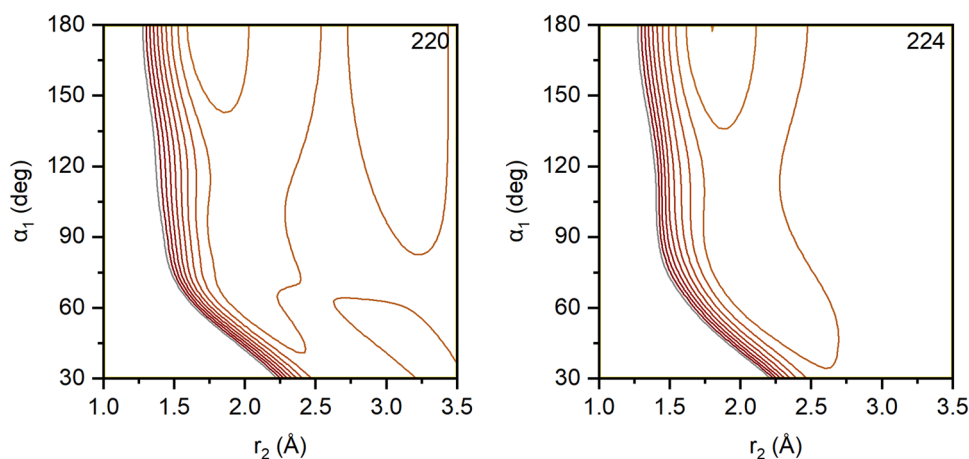


FIG. 7. Contour map of $6A'$ potential of NO_2 , where $r_3 = 1.151 \text{ \AA}$. The increment in the contours is 10 kcal/mol; the energies are 0 kcal/mol–300 kcal/mol (left—MEG, right—NN). The energy of the plateau is added at the upper right corner.

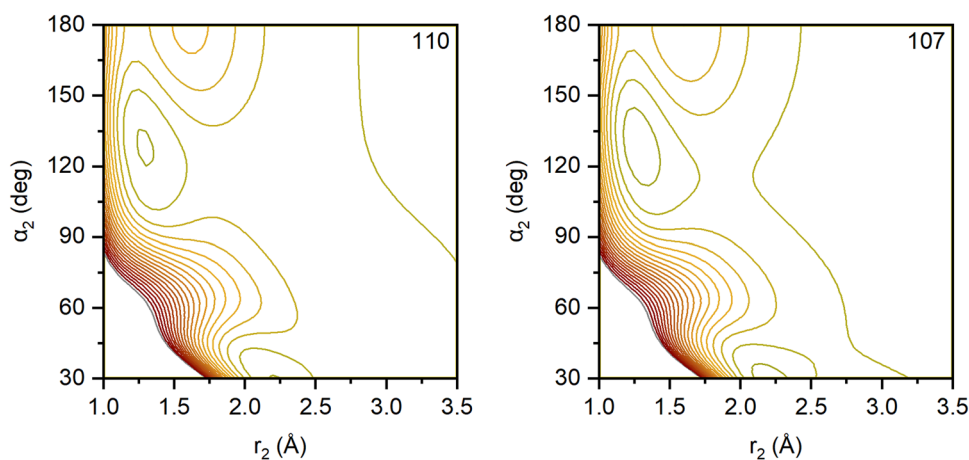


FIG. 8. Contour map of $2A'$ potential of NO_2 , where $r_1 = 1.208 \text{ \AA}$. The increment in the contours is 10 kcal/mol; the energies are 0 kcal/mol–300 kcal/mol (left—MEG, right—NN). The energy of the plateau is added at the upper right corner.

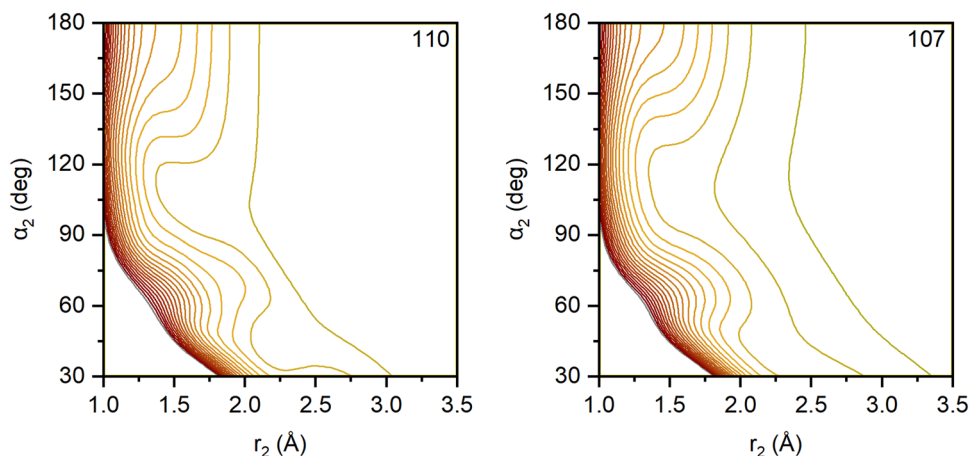


FIG. 9. Contour map of $4A'$ potential of NO_2 , where $r_1 = 1.208$ Å. The increment in the contours is 10 kcal/mol; the energies are 0 kcal/mol–300 kcal/mol (left—MEG, right—NN). The energy of the plateau is added at the upper right corner.

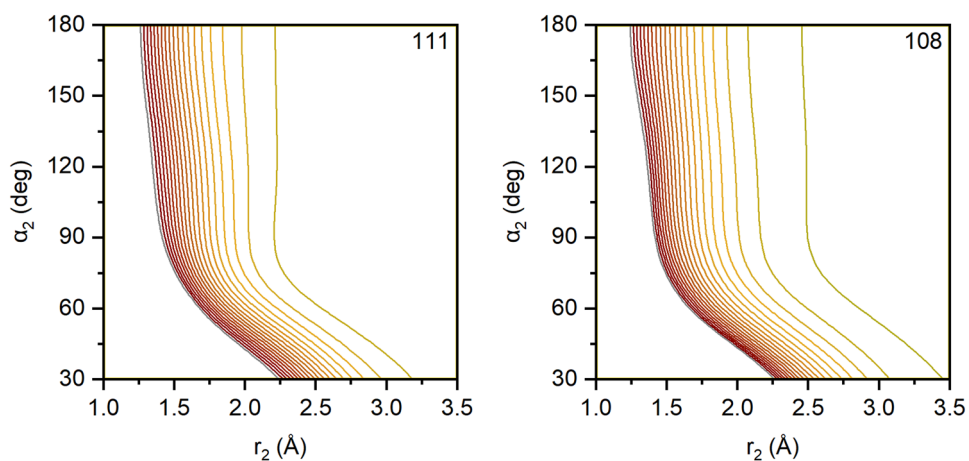


FIG. 10. Contour map of $6A'$ potential of NO_2 , where $r_1 = 1.208$ Å. The increment in the contours is 10 kcal/mol; the energies are 0 kcal/mol–300 kcal/mol (left—MEG, right—NN). The energy of the plateau is added at the upper right corner.

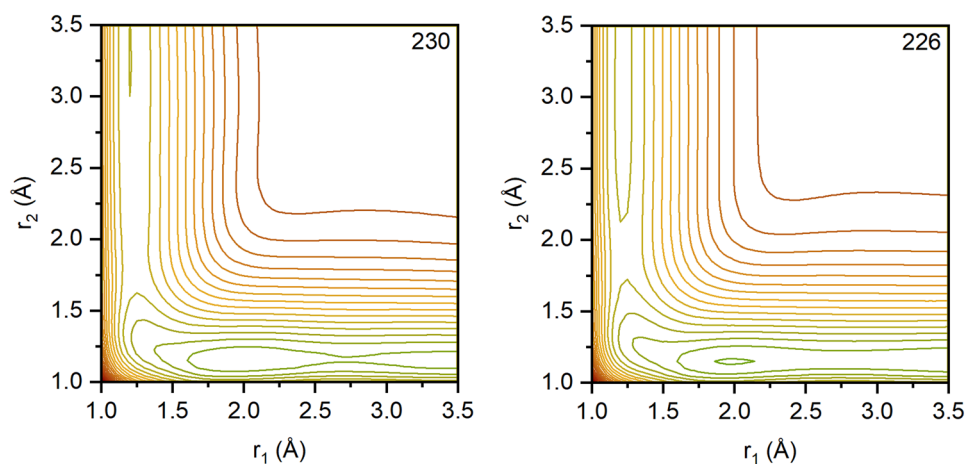


FIG. 11. Contour map of $2A'$ potential of NO_2 , where $\alpha_2 = 120^\circ$. The increment in the contours is 10 kcal/mol; the energies are 0 kcal/mol–300 kcal/mol (left—MEG, right—NN). The energy of the plateau is added at the upper right corner.

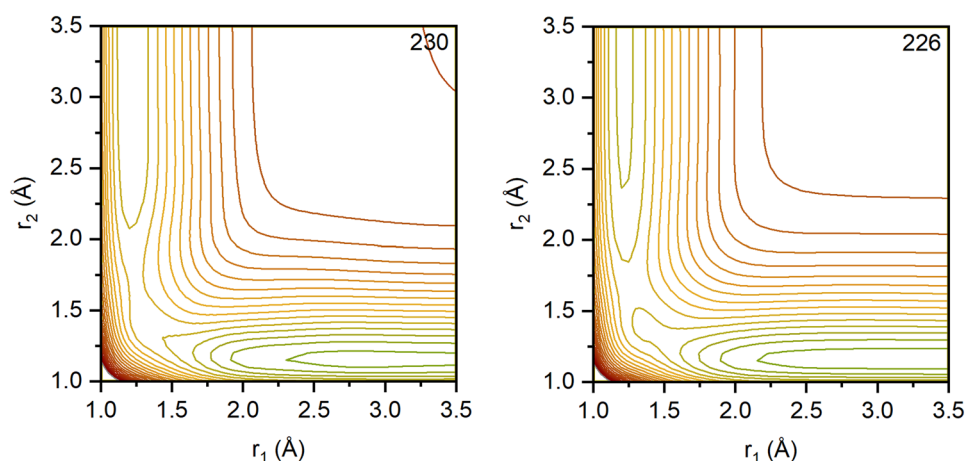


FIG. 12. Contour map of $4A'$ potential of NO_2 , where $\alpha_2 = 120^\circ$. The increment in the contours is 10 kcal/mol; the energies are 0 kcal/mol–300 kcal/mol (left—MEG, right—NN). The energy of the plateau is added at the upper right corner.

distances; thus, it is not shown in the plots of Fig. 4. For the sextet state, the top of the barrier between the NO_2 region and the region of $\text{O}_2 + \text{N}$ is higher in energy than the barriers for the doublet and quartet surfaces. This is a transition structure by the MB-PIP-MEG fit, but it is a second-order transition structure by the PIP-NN fit. For this reason, this structure is denoted as S3-(s)ts in Table X to reflect both possibilities.

In Figs. 5($^2A'$), 6($^4A'$), and 7($^6A'$), the α_1 angle is varied from 30° to 180° and one of the two N–O distances (r_2) is varied from 1.0 to 3.5 Å, while the other N–O distance (r_3) is fixed at 1.151 Å. Just like Fig. 2, Fig. 5 contains the well of 2A_1 structures (D1-min) since it is lower in energy than the plateau, which corresponds to $\text{NO}(^2\Pi) + \text{O}(^3\text{P})$. Since the well region of the quartet surface in Fig. 3 is higher in energy than the energy of $\text{NO}(^2\Pi) + \text{O}(^3\text{P})$, the well mainly disappears in Fig. 6. The sextet surface, Fig. 7, is many repulsive, and the plateau lies much higher in energy than those of the doublet and quartet surfaces due to the quartet spin state of $\text{NO}(^4\Pi)$.

In Figs. 8($^2A'$), 9($^4A'$), and 10($^6A'$), the α_2 angle is varied from 30° to 180° and one of the two N–O distances (r_2) is varied from

1.0 Å to 3.5 Å, while the O–O distance (r_1) is fixed at 1.208 Å. The doublet surface (Fig. 8) has two small wells in this cut around $\alpha_2 = 125^\circ$ and $r_2 = 1.3$ Å, as well as $\alpha_2 = 30^\circ$ and $r_2 = 2.2$ Å. Both wells are part of the well of the same NOO structure (D5-min); the difference is only the order of the atoms. This cut also has a hill surface feature around $\alpha_2 = 180^\circ$ and $r_2 = 1.6$ Å, which belongs to structure D6-sts. The quartet (Fig. 9) and sextet (Fig. 10) surfaces are mainly repulsive for this cut.

In Figs. 11($^2A'$), 12($^4A'$), and 13($^6A'$), the α_2 angle is fixed at 120° , and the O–O distance (r_1) and one of the two N–O distances (r_2) are varied from 1.0 Å to 3.5 Å. The doublet and quartet surfaces are again very similar since both the $\text{O}_2(^3\Sigma_g^-) + \text{N}(^4\text{S})$ and the $\text{NO}(^2\Pi) + \text{O}(^3\text{P})$ channels appear in both spin states. In the sextet surface, the channel of $\text{O}_2(^3\Sigma_g^-) + \text{N}(^4\text{S})$ is still there, but in the other channel, $\text{O}(^3\text{P})$ has to combine with $\text{NO}(^4\Pi)$; thus, it has higher energy than the doublet or quartet surfaces.

The computational cost using the surfaces is an important factor in dynamics simulations. To compare the compute times of the NN and MEG fits, we used the data from the second series of

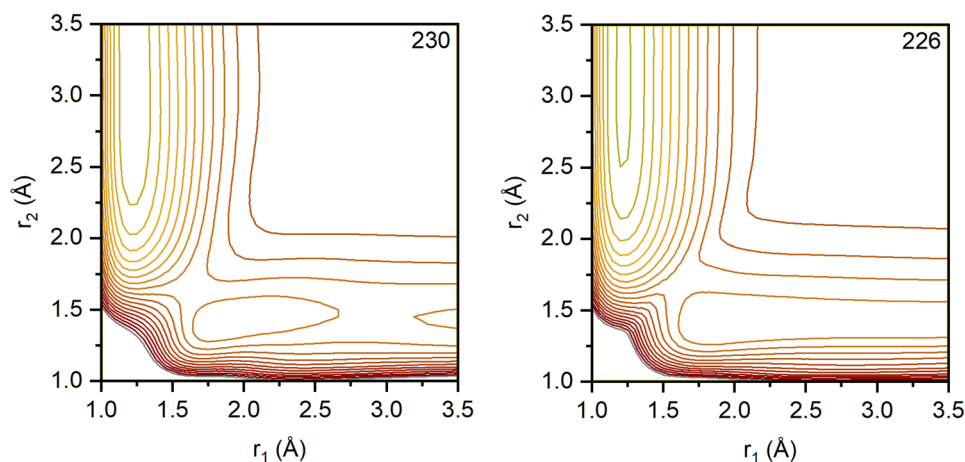


FIG. 13. Contour map of $6A'$ potential of NO_2 , where $\alpha_2 = 120^\circ$. The increment in the contours is 10 kcal/mol; the energies are 0 kcal/mol–300 kcal/mol (left—MEG, right—NN). The energy of the plateau is added at the upper right corner.

trajectory calculations described in Sec. II C, where 1100 trajectories were run for each of the six surfaces. Both the NN and the MEG subroutines have analytical gradients, and those were used (unlike the case for the N_4 system,⁵⁶ for NO_2 , the evaluation of the analytical gradients⁸⁹ of the neural network fit is faster than the evaluation of numerical gradients). We know from a similar comparison made for N_4 system⁵⁶ that if the Bulirsch–Stoer integrator with adaptive step size is used in trajectory propagation, then the cost ratio of the trajectories is dominated by the cost of calculating the gradients. Averaging over the whole second series of trajectories (3300 trajectories for each fitting method), we found that the average compute time for NN trajectories is 4.9 times larger than that for MEG trajectories (a ratio of 4.6 for the doublet, 5.0 for the quartet, and 5.2 for the sextet). The ratio of compute times is closer to unity for NO_2 than for N_4 , where the ratio of compute time for NN to MEG was about 17.⁵⁶ However, in the MEG fits of NO_2 , we use a higher-order polynomial (12th order) than that used for N_4 (9th order); thus, the lower ratio of compute times in the present work is, at least, partially due to making the MEG fit more expensive.

V. SUMMARY

In this work, we provide potential energy surfaces for studying high-energy collisions between nitrogen atoms and oxygen molecules. The doublet, quartet, and sextet A' surfaces presented here are suitable for collisions of $O_2(^3\Sigma_g^-)$ with $N(^4S)$. The surfaces were fitted two ways, using both the MB-PIP-MEG method and the PIP-NN method against datasets with DSEC-corrected CASPT2//DW-SA(3)-CASSCF(12o,17e) calculations. The neural network fit has superior performance to MB-PIP-MEG, although its gradient evaluation for trajectory simulations is 5 times more expensive than the gradient of MB-PIP-MEG.

SUPPLEMENTARY MATERIAL

The [supplementary material](#) contains the fitting datasets of the doublet, quartet, and sextet A' potential energy surfaces of NO_2 , the subroutines of the MB-PIP-MEG and the PIP-NN fits of the surfaces (which provide both the energy and the gradients calculated analytically), and two examples of *Molpro* input files.

ACKNOWLEDGMENTS

Continuing discussions with Tom Schwartztruber and Graham Candler are greatly appreciated. Computational resources were provided by the Department of Aerospace Engineering and Mechanics at the University of Minnesota and by the Minnesota Supercomputing Institute. The work of Y.L. and J.L. was supported by the National Natural Science Foundation of China (Grant No. 21973009) and the Chongqing Municipal Natural Science Foundation (Grant No. cstc2019jcyj-msxmX0087). The work of H.G. and D.G.T. was supported by the U. S. Department of Energy, Office of Science, Office of Basic Energy Sciences, under Award No. DE-SC0015997.

DATA AVAILABILITY

The data that support the findings of this study are available within the article in the [supplementary material](#). The potential energy surfaces are also available in *Potlib*: <http://comp.chem.umn.edu/potlib/>.

REFERENCES

- ¹M. B. McElroy, M. J. Prather, and J. M. Rodriguez, *Geophys. Res. Lett.* **9**, 649, <https://doi.org/10.1029/GL009i006p00649> (1982).
- ²A. F. Nagy, J. Kim, T. E. Cravens, and A. J. Kliore, *Geophys. Res. Lett.* **25**, 4153, <https://doi.org/10.1029/1998gl900139> (1998).
- ³J. L. Ollivier, M. Dobrićević, and J. P. Parisot, *Planet. Space Sci.* **48**, 699 (2000).
- ⁴A. Eviatar, V. M. Vasyliūnas, and D. A. Gurnett, *Planet. Space Sci.* **49**, 327 (2001).
- ⁵Y. L. Yung, M. Liang, G. A. Blake, R. P. Muller, and C. E. Miller, *Geophys. Res. Lett.* **31**, L19106, <https://doi.org/10.1029/2004GL020950> (2004).
- ⁶V. Kharchenko and A. Dalgarno, *J. Geophys. Res.: Atmos.* **109**, D18311, <https://doi.org/10.1029/2004jd004597> (2004).
- ⁷V. N. Azyazov and M. C. Heaven, *Int. J. Chem. Kinet.* **47**, 93 (2015).
- ⁸Z.-C. Wang and V. M. Bierbaum, *J. Chem. Phys.* **144**, 214304 (2016).
- ⁹Y. Sun, F. Xu, X. Li, Q. Zhang, and Y. Gu, *Phys. Chem. Chem. Phys.* **21**, 21856 (2019).
- ¹⁰M. Panesi, R. L. Jaffe, D. W. Schwenke, and T. E. Magin, *J. Chem. Phys.* **138**, 044312 (2013).
- ¹¹M. Panesi, A. Munafò, T. E. Magin, and R. L. Jaffe, *Phys. Rev. E* **90**, 013009 (2014).
- ¹²D. Andrienko and I. D. Boyd, *Chem. Phys.* **459**, 1 (2015).
- ¹³D. A. Andrienko and I. D. Boyd, *J. Chem. Phys.* **145**, 014309 (2016).
- ¹⁴P. Valentini, T. E. Schwartztruber, J. D. Bender, and G. V. Candler, *Phys. Rev. Fluids* **1**, 043402 (2016).
- ¹⁵R. Celiberto *et al.*, *Plasma Sources Sci. Technol.* **25**, 033004 (2016).
- ¹⁶D. A. Andrienko and I. D. Boyd, *Chem. Phys.* **491**, 74 (2017).
- ¹⁷R. L. Macdonald, R. L. Jaffe, D. W. Schwenke, and M. Panesi, *J. Chem. Phys.* **148**, 054309 (2018).
- ¹⁸D. A. Andrienko and I. D. Boyd, *J. Chem. Phys.* **148**, 084309 (2018).
- ¹⁹R. S. Chaudhry, J. D. Bender, T. E. Schwartztruber, and G. V. Candler, *J. Thermophys. Heat Transfer* **32**, 833 (2018).
- ²⁰T. E. Schwartztruber, M. S. Grover, and P. Valentini, *J. Thermophys. Heat Transfer* **32**, 892 (2018).
- ²¹D. A. Andrienko and I. D. Boyd, *J. Thermophys. Heat Transfer* **32**, 904 (2018).
- ²²N. Singh and T. Schwartztruber, *Proc. Natl. Acad. Sci. U. S. A.* **115**, 47 (2018).
- ²³M. S. Grover, T. E. Schwartztruber, Z. Varga, and D. G. Truhlar, *J. Thermophys. Heat Transfer* **33**, 797 (2019).
- ²⁴J. D. Bender, P. Valentini, I. Nompelis, Y. Paukku, Z. Varga, D. G. Truhlar, T. Schwartztruber, and G. V. Candler, *J. Chem. Phys.* **143**, 054304 (2015).
- ²⁵Y. Paukku, K. R. Yang, Z. Varga, G. Song, J. D. Bender, and D. G. Truhlar, *J. Chem. Phys.* **147**, 034301 (2017).
- ²⁶Y. Paukku, Z. Varga, and D. G. Truhlar, *J. Chem. Phys.* **148**, 124314 (2018).
- ²⁷Z. Varga, R. Meana-Pañeda, G. Song, Y. Paukku, and D. G. Truhlar, *J. Chem. Phys.* **144**, 024310 (2016).
- ²⁸W. Lin, Z. Varga, G. Song, Y. Paukku, and D. G. Truhlar, *J. Chem. Phys.* **144**, 024309 (2016).
- ²⁹Z. Varga, Y. Paukku, and D. G. Truhlar, *J. Chem. Phys.* **147**, 154312 (2017).
- ³⁰D. G. Truhlar, *J. Chem. Phys.* **56**, 3189 (1972).
- ³¹K. Yoshino, J. R. Esmond, and W. H. Parkinson, *Chem. Phys.* **221**, 169 (1997).
- ³²T. C. Corcoran, E. J. Beiting, and M. O. Mitchell, *J. Mol. Spectrosc.* **154**, 119 (1992).
- ³³S. A. Tashkun and P. Jensen, *J. Mol. Spectrosc.* **165**, 173 (1994).
- ³⁴H. Vilanove and M. Jacon, *Int. J. Quantum Chem.* **55**, 419 (1995).
- ³⁵A. J. C. Varandas and A. I. Voronin, *Mol. Phys.* **85**, 497 (1995).

- ³⁶E. Leonardi, C. Petrongolo, G. Hirsch, and R. J. Buenker, *J. Chem. Phys.* **105**, 9051 (1996).
- ³⁷D. Xie and G. Yan, *Mol. Phys.* **88**, 1349 (1996).
- ³⁸J. H. Schryber, O. L. Polyansky, P. Jensen, and J. Tennyson, *J. Mol. Spectrosc.* **185**, 234 (1997).
- ³⁹R. F. Salzgeber, V. Mandelshtam, C. Schlier, and H. S. Taylor, *J. Chem. Phys.* **109**, 937 (1998).
- ⁴⁰S. Y. Grebenshchikov, C. Beck, H. Flöthman, R. Schinke, and S. Kato, *J. Chem. Phys.* **111**, 619 (1999).
- ⁴¹S. Mahapatra, H. Köppel, L. S. Cederbaum, P. Stampfuß, and W. Wenzel, *Chem. Phys.* **259**, 211 (2000).
- ⁴²M. Braunstein and J. W. Duff, *J. Chem. Phys.* **113**, 7406 (2000).
- ⁴³D. Reignier, T. Stoecklin, P. Halvick, A. Voronin, and J. C. Rayez, *Phys. Chem. Chem. Phys.* **3**, 2726 (2001).
- ⁴⁴H. J. Kim and Y. S. Kim, *Bull. Korean Chem. Soc.* **22**, 455 (2001).
- ⁴⁵R. Sayós, C. Oliva, and M. González, *J. Chem. Phys.* **117**, 670 (2002).
- ⁴⁶V. Kurkal, P. Fleurat-Lessard, and R. Schinke, *J. Chem. Phys.* **119**, 1489 (2003).
- ⁴⁷A. J. C. Varandas, *J. Chem. Phys.* **119**, 2596 (2003).
- ⁴⁸V. C. Mota, P. J. S. B. Caridade, and A. J. C. Varandas, *Int. J. Quantum Chem.* **111**, 3776 (2011).
- ⁴⁹J. C. Castro-Palacio, T. Nagy, R. J. Bemish, and M. Meuwly, *J. Chem. Phys.* **141**, 164319 (2014).
- ⁵⁰B. J. Braams and J. M. Bowman, *Int. Rev. Phys. Chem.* **28**, 577 (2009).
- ⁵¹Z. Xie and J. M. Bowman, *J. Chem. Theory Comput.* **6**, 26–34 (2010).
- ⁵²Y. Paukku, K. R. Yang, Z. Varga, and D. G. Truhlar, *J. Chem. Phys.* **139**, 044309 (2013).
- ⁵³B. Jiang and H. Guo, *J. Chem. Phys.* **139**, 054112 (2013).
- ⁵⁴J. Li, B. Jiang, and H. Guo, *J. Chem. Phys.* **139**, 204103 (2013).
- ⁵⁵B. Jiang, J. Li, and H. Guo, *Int. Rev. Phys. Chem.* **35**, 479 (2016).
- ⁵⁶J. Li, Z. Varga, D. G. Truhlar, and H. Guo, *J. Chem. Theory Comput.* **16**, 4822 (2020).
- ⁵⁷H.-J. Werner, P. J. Knowles, G. Knizia, F. R. Manby, and M. Schütz, *Wiley Interdiscip. Rev.: Comput. Mol. Sci.* **2**, 242 (2012).
- ⁵⁸H.-J. Werner, P. J. Knowles, G. Knizia, F. R. Manby, M. Schütz, P. Celani, T. Korona, R. Lindh, A. Mitrushenkov, G. Rauhut, K. R. Shamasundar, T. B. Adler, R. D. Amos, A. Bernhardsson, A. Berning, D. L. Cooper, M. J. O. Deegan, A. J. Dobbyn, F. Eckert, E. Goll, C. Hampel, A. Hesselmann, G. Hetzer, T. Hrenar, G. Jansen, C. Köppl, Y. Liu, A. W. Lloyd, R. A. Mata, A. J. May, S. J. McNicholas, W. Meyer, M. E. Mura, A. Nicklass, D. P. O'Neill, P. Palmieri, D. Peng, K. Pflüger, R. Pitzer, M. Reiher, T. Shiozaki, H. Stoll, A. J. Stone, R. Tarroni, T. Thorsteinsson, and M. Wang, *Molpro*, version 2012.1, a package of *ab initio* programs, <http://www.molpro.net>.
- ⁵⁹M. P. Deskevich, D. J. Nesbitt, and H.-J. Werner, *J. Chem. Phys.* **120**, 7281 (2004).
- ⁶⁰K. K. Docken and J. Hinze, *J. Chem. Phys.* **57**, 4928 (1972); R. N. Diffenderfer and D. R. Yarkony, *J. Phys. Chem.* **86**, 5098 (1982); H. J. Werner and W. Meyer, *J. Chem. Phys.* **74**, 5794 (1981).
- ⁶¹K. Ruedenberg, L. M. Cheung, and S. T. Elbert, *Int. J. Quantum Chem.* **16**, 1069 (1979); B. O. Roos, *Int. J. Quantum Chem. Symp.* **14**, 175 (1980); K. Ruedenberg, M. W. Schmidt, M. M. Gilbert, and S. T. Elbert, *Chem. Phys.* **71**, 41 (1982).
- ⁶²H. J. Werner and P. J. Knowles, *J. Chem. Phys.* **82**, 5053 (1985); P. J. Knowles and H.-J. Werner, *Chem. Phys. Lett.* **115**, 259 (1985).
- ⁶³H.-J. Werner, *Mol. Phys.* **89**, 645 (1996).
- ⁶⁴B. O. Roos and K. Andersson, *Chem. Phys. Lett.* **245**, 215 (1995).
- ⁶⁵See <https://www.molpro.net> for Molpro Manual.
- ⁶⁶For the theory of modified Fock operators, see K. Andersson, *Theor. Chim. Acta* **91**, 31 (1995).
- ⁶⁷E. Papajak, H. R. Leverentz, J. Zheng, and D. G. Truhlar, *J. Chem. Theory Comput.* **5**, 1197 (2009).
- ⁶⁸F. B. Brown and D. G. Truhlar, *Chem. Phys. Lett.* **117**, 307 (1985).
- ⁶⁹H. Okabe, *Photochemistry of Small Molecules* (Wiley, New York, 1978).
- ⁷⁰See <http://cccbdb.nist.gov> for NIST Computational Chemistry Comparison and Benchmark Database.
- ⁷¹D. Steele, E. R. Lippincott, and J. T. Vanderslice, *Rev. Mod. Phys.* **34**, 239 (1962).
- ⁷²J. Zheng, Z.-H. Li, A. W. Jasper, D. A. Bonhommeau, R. Valero, R. Meana-Pañeda, S. L. Mielke, L. Zhang, and D. G. Truhlar, ANT, version 2019, University of Minnesota, Minneapolis, 2019, <http://comp.chem.umn.edu/ant>.
- ⁷³C. Qu, Q. Yu, and J. M. Bowman, *Annu. Rev. Phys. Chem.* **69**, 151 (2018).
- ⁷⁴J. M. Raff, R. Komanduri, M. Hagan, and S. T. S. Bukkapatnam, *Neural Networks in Chemical Reaction Dynamics* (Oxford University Press, Oxford, 2012).
- ⁷⁵Z.-H. Zhou, J. Wu, and W. Tang, *Artif. Intell.* **137**, 239 (2002).
- ⁷⁶P. Valentini, M. S. Grover, and E. Josyula, *Phys. Rev. E* **102**, 053302 (2020).
- ⁷⁷S. Grimme, J. Antony, S. Ehrlich, and H. Krieg, *J. Chem. Phys.* **132**, 154104 (2010).
- ⁷⁸S. Grimme, S. Ehrlich, and L. Goerigk, *J. Comput. Chem.* **32**, 1456 (2011).
- ⁷⁹P. Verma, B. Wang, L. E. Fernandez, and D. G. Truhlar, *J. Phys. Chem. A* **121**, 2855 (2017).
- ⁸⁰L. Bytautas, N. Matsunaga, and K. Ruedenberg, *J. Chem. Phys.* **132**, 074307 (2010).
- ⁸¹K. P. Huber and G. Herzberg, *Molecular Spectra Molecular Structure IV. Constants of Diatomic Molecules* (Van Nostrand Reinhold, New York, 1979).
- ⁸²Y. Paukku, K. R. Yang, Z. Varga, and D. G. Truhlar, *J. Chem. Phys.* **139**, 044309 (2013).
- ⁸³K. R. Yang, Z. Varga, and D. G. Truhlar, *PIPFit—Version 2015* (University of Minnesota, Minneapolis, 2015).
- ⁸⁴G. Cybenko, *Math. Control Signals Syst.* **2**, 303 (1989).
- ⁸⁵J. B. Witkoskie and D. J. Doren, *J. Chem. Theory Comput.* **1**, 14 (2005).
- ⁸⁶J. M. Raff, R. Komanduri, M. Hagan, and S. T. S. Bukkapatnam, *Neural Networks in Chemical Reaction Dynamics* (Oxford University Press, Oxford, 2012).
- ⁸⁷J. Behler, *J. Phys.: Condens. Matter* **26**, 183001 (2014).
- ⁸⁸J. Zheng, S. Zhang, B. J. Lynch, J. C. Corchado, Y.-Y. Chuang, P. L. Fast, W.-P. Hu, Y.-P. Liu, G. C. Lynch, K. A. Nguyen, C. F. Jackels, A. Fernandez Ramos, B. A. Ellingson, V. S. Melissas, J. Villà, I. Rossi, E. L. Coitiño, J. Pu, T. V. Albu, R. Steckler, B. C. Garrett, A. D. Isaacson, and D. G. Truhlar, *POLYRATE—version 2010–A*, University of Minnesota, Minneapolis, 2010, <https://comp.chem.umn.edu/polyrate/>.
- ⁸⁹D. Lu and J. Li, “Full-dimensional global potential energy surfaces describing abstraction and exchange for the H + H₂S reaction,” *J. Chem. Phys.* **145**, 014303 (2016).
- ⁹⁰R. J. Duchovic, Y. L. Volobuev, G. C. Lynch, T. C. Allison, J. C. Corchado, D. G. Truhlar, A. F. Wagner, and B. C. Garrett, “POTLIB 2001: A potential energy surface library for chemical systems,” *Comput. Phys. Commun.* **144**, 169 (2002); “POTLIB 2001: A potential energy surface library for chemical systems,” **156**, 319 (2004).
- ⁹¹The six new NO₂ potential energy surface subroutines presented here (three MB-PIP-MEG and three PIP-NN) are available in the updated POTLIB library at <http://comp.chem.umn.edu/potlib/>.